Title:
A Coherent Method for Simulating Active and Passive Radar Sounding of the Jovian Icy Moons

This paper appears in:
IEEE Transactions on Geoscience and Remote Sensing

Date of Publication:
2019

Author(s):
Christopher Gerekos, Lorenzo Bruzzone, Masafumi Imai

DOI:
10.1109/TGRS.2019.2945079

A coherent method for simulating active and passive radar sounding of the Jovian icy moons

Christopher Gerekos, Lorenzo Bruzzone, *Fellow, IEEE*, and Masafumi Imai

***Abstract*—The possibility to apply passive radar sounding techniques to the Jovian icy moons, making use of Jupiter's strong decametric emissions (DAM), has recently garnered large research interest. In this paper, we propose a radar sounding simulation approach being able to simulate and compare passive and active acquisitions for a given scenario. The proposed simulator is based on the Stratton-Chu integral used with the linear phase approximation on triangular facets. The external field is modelled with plane waves, the direction, polarisation, and amplitude of which can be freely chosen. The time-domain dependence can be either synthetically generated (*e.g.*, Gaussian white noise), or taken from experimental measurements (*e.g.*, waveforms recorded by a radio telescope observing Jupiter). For passive sounding, both autocorrelation and cross-correlation processing is considered. Validation tests were conducted on a series of ideal digital elevation models, such as flat surfaces and subsurfaces, or gaussian rough surfaces, and a good agreement with the existing literature was obtained. To illustrate the capabilities of the proposed simulator, we conducted additional, more realistic experiments of radar sounding simulations, where we use both white noise and Jovian waveforms recorded by the LWA1 radio telescope.**

***Index Terms*—Radar sounder, simulations, passive sounding, Europa, Ganymede, decametric emissions**

I. Introduction

RADAR sounders operate by recording the reflections of electromagnetic waves from a given solid planetary object. The incoming field may come either from the receiving radar itself, a mode of operation known as *monostatic active sounding*, either from another radar instrument at a different location, in which case the mode of acquisition is called *bistatic active sounding*; lastly, if the incoming field is generated by an external source with *a priori* unknown properties, the process is known as *passive sounding* [33]. Passive sounding can be performed with opportunity signals coming from one (*e.g.*, [16]) or several external sources (*e.g.*, [22]). Reflections are produced when this incoming field encounters abrupt changes of the dielectric constant across the propagation volume, such as the surface of the body, possible subsurface layers, and/or discrete diffractors within the subsurface. By analysing the properties of the reflected fields, it is possible to infer many physical characteristics of the targeted body, such as its surface topography or subsurface composition. Examples of scientifically successful spaceborne radar sounders include the Mars Advanced Radar for Subsurface and Ionosphere Sounding (MARSIS) onboard ESA's Mars Express probe [27], the Shallow Radar (SHARAD) instrument onboard NASA's Mars Reconnaissance Orbiter [32], and the Lunar Radar Sounder (LRS) onboard JAXA's Kaguya probe [25].

The three icy moons of Jupiter, Europa, Ganymede, and Callisto, are high-value science targets for radar sounders. There is a growing body of indirect evidence that they harbour global liquid water oceans under their icy crust [18][34]. The depth of this ocean is though to be greater that 80 km for Ganymede and Callisto, which is too deep for a radar sounder to detect directly, and from a few kilometres to a few tens of kilometres for Europa, making it possibly directly detectable. It is also thought that Europa and Ganymede might have shallow liquid water pockets at depths of a few kilometres [15]. Over the next decade, two major planetary science missions will be launched towards the Jovian system, both having radar sounder instruments in their payloads: the Radar for Icy Moons Exploration (RIME) onboard the ESA's Jupiter Icy Moons Explorer (JUICE) spacecraft [6], and the Radar for Europa Assessment and Sounding: Ocean to Near-Surface (REASON), embarked on NASA's Europa Clipper probe [5]. The former has a central frequency of 9 MHz and a selectable bandwidth of 1 MHz or 2.8 MHz, the latter is a dual-frequency instrument emitting signals centred at 9 and 60 MHz, with 1 MHz and 10 MHz bandwidth, respectively. RIME will make acquisitions on Europa, Ganymede and Callisto, whereas REASON will focus on Europa

One of the main technical challenges that RIME and the low-frequency sounder of REASON must overcome is the hostile Jovian radio environment, characterised by strong sporadic emissions. Around 9 MHz, these radio emissions share the decametric (DAM) radio component (comprising Io-related DAM and non-Io-related DAM) between a few MHz and 40 MHz, and the hectometeric (HOM) component between 300 kHz and 10 MHz [7][38][17]. These sources commonly originate from Jupiter's poles. Their spectral flux density can reach 10^{-14} W/m^2/Hz at Europa, the icy moon closest to Jupiter, which is about five orders of magnitude higher than the galactic background [9]. Earth-based radio telescopes have been observing DAM radiation for several decades at frequencies no lower than 10 MHz, due to the terrestrial ionosphere and radio frequency interferences. In contrast, the full spectrum of HOM radiation is accessible from space-based radio observations. Planetary science spacecraft are able to synoptically record the entire Jovian DAM spectrum (Voyager and Juno) or the lower frequency part of the DAM spectrum

C. Gerekos and L. Bruzzone are with the Department of Information Engineering and Computer Science, University of Trento, 38123 Trento, Italy (e-mail: christopher.gerekos@unitn.it; lorenzo.bruzzone@ing.unitn.it), M. Imai is with the Department of Physics and Astronomy, University of Iowa, IA 52242, USA.

Accepted 27 September 2019.

below 16 MHz (Galileo, Ulysses, and Cassini) [21][37].

Several strategies have been devised to mitigate the effect of these emissions on the two Jovian sounders: for REASON, the presence of the 60 MHz sounding mode ensures measurements are possible outside the main Jovian noise frequencies, and for RIME, the instrument is currently planned to operate mainly on the anti-Jovian side of the moons. However, recent papers have highlighted the possibility to use those emissions to perform passive sounding. The idea was first proposed in [29], where the authors derived the properties of the autocorrelation functions of the Jovian emissions as a function of, amongst others, the backscattering geometry and some subsurface properties. In [31], the signal-to-noise ratio (SNR) and signal-to-clutter ratio (SCR) of active and passive acquisitions are compared using the radar equation. In [20], the feasibility of passive interferometrical sounding is investigated for JUICE's Radio and Plasma Wave Investigation (RPWI) instrument. However, those studies have relied on one-dimensional modelling and did not consider the specific implications of the different scenarios on the acquired radargrams in a given target area (for instance, in [31], roughness was simply treated as an additional geometrical spreading factor). Additionally, the Jovian emissions were modelled as white noise, whereas the Jovian emissions have a more complex spectrum, which potentially has an impact on the quality of passive sounding acquisitions [8].

In this paper, we propose a method to accurately simulate radar echoes from the surface and the subsurface of a given planetary body (*e.g.*, Ganymede and Europa), in both active and passive modes. The proposed algorithm takes into account a great range of radar parameters such as the power, central frequency, bandwidth, as well as the altitude of the instrument, its antenna pattern, and the duration of its listening window. The simulator is based on the multilayer Stratton-Chu simulator presented in [14], which was developed for simulating noise-free monostatic active acquisitions. Simulation of passive signals is done by modelling the external source of radiation as plane waves, where the amplitude, polarisation and time dependence can be chosen freely. The passive signal can thus be chosen fit a particular type of emission, such as Jovian auroral radiation. Similarly, the time-dependence can be either synthetically generated (*e.g.*, with Gaussian signals) or derived from actual measurements. The simulator can also model the effect of external sources of radiation in active acquisitions by considering an external field determined from the same aforementioned parameters. Not that by taking the same external field in passive and active acquisition modes, we can study a given scenario and analyze the differences between (i) noise-free active sounding, (ii) noisy active sounding and (iii) passive sounding in otherwise identical conditions. Thus the proposed method is a valuable tool in determining the relative scientific value of each sounding mode.

The proposed technique for noisy active and passive sounding simulations is validated in a series of controlled setups. Simulations with homogeneous flat layers are compared to the radar equation, simulations with gaussian surface roughness are compared to the "geometrical spreading factor" of [31], whereas the effect of the listening window length is investigated on a digital elevation model (DEM) including fractal rough layers. In all cases a very satisfactory agreement with the literature was obtained. Lastly, as an illustration of the capabilities of the simulator, we perform simulations based on DEMs of Martian areas that are good analogues of terrains of Ganymede and Europa. Both Gaussian and experimentally-acquired samples of the Jovian noise are used, which visually highlight the effects of the non-whiteness of the Jovian emissions on the radargrams.

This paper is structured as follows. Section II recalls the basic principles behind passive sounding and the properties of common noise models. In section III we extensively develop the scattering equations that we are proposing to simulate passive and active acquisitions. In section IV, the post-processing of the acquired electromagnetic fields is described. Section V details the validation tests that we conducted and shows the proposed simulator is reacting as expected. Section VI presents the results obtained with the proposed method in realistic sounding scenarios of the Jovian icy moons. Lastly, section VII draws the conclusions of this paper.

Throughout this paper, quantities in bold represent vectors. Unless otherwise mentioned, the same quantities in normal font represent their norm. Hatted vectors represent vectors of unit norm.

II. Passive sounding fundamentals

In this section we review the properties of passive sounding acquisitions with different types of noise. Two main strategies can be used to perform passive sounding with a radar instrument. The first one is to use the radar in receiving mode for an extended period and to perform an autocorrelation analysis of the recorded signal to reveal possible features. The second one involves switching on the receiver twice for restricted amounts of time: a first time to record the "incoming" signal (this replaces the original transmitting window in active sounding), and a second time, later on, to record the reflected signals (this corresponds to the nominal receiving window) [36]. The gap between those two listening windows depends on the pre-estimated range of the echoes. In this case, the possible reflections are uncovered by cross-correlating the recorded incoming signal with the subsequent recorded echoes.

The SNR of a passive acquisition typically increases with the duration of the acquisition [1]. However, orbital platforms are limited by their own movement: if the acquisition lasts for too long, the echoes from the beginning of the acquisition will not come from the same region as those at the end of it, leading to a mixing of the echoes from different scenes and to a loss of SNR. They should thus typically operate on shorter, repeated windows. Stationary sounders (for instance, mounted on a lander) are not limited by this constrain, and can collect signals indefinitely to increase their SNR [28][26]. Thus, the autocorrelation method is preferable for stationary sounders, while the cross-correlation method is preferred on orbital sounders.

For simplicity, we assume in this section that all fields are scalar; vectorial treatment is considered later on, in the description of the proposed simulator of Sec. III. We introduce

the following notation. Given two complex scalar functions $a(t)$ and $b(t)$, we define the *cross-correlation* of a and b as

$$a(t) \otimes b(t) \equiv \int_{-\infty}^{\infty} a(t')b^{\dagger}(t'-t)dt', \tag{1}$$

where the dagger symbolises the complex-conjugate of the signal. The *autocorrelation* of a is obtained by setting $b(t) \equiv a(t)$. In practice, the correlation is performed over a finite time T.

Let $s_{\text{noise}}(t)$ be the external signal as it arrives at the receiver. Every reflector n in the considered volume will generate a signal given by $s_n(t) = A_n s_{\text{noise}}(t-\tau_n)$, that is, a copy of the original signal scaled by a factor $A_n \leq 1$ and shifted by a delay τ_n (phase changes are neglected in this simplified model, but they are obviously considered in the backscattering simulations). Assuming an arbitrary number N of reflectors, which can be geological components of the target body, the total signal is given by $s_{tot} = \sum_{n=0}^{N} A_n s_{\text{noise}}(t-\tau_n)$, with $A_0 = 1$ and $\tau_0 = 0$.

A. Autocorrelation method

Let $S(t)$ be the autocorrelation function of $s_{\text{noise}}(t)$. The autocorrelation of the total signal $S_{tot}(t) = s_{tot}(t) \otimes s_{tot}(t)$ is given by:

$$S_{tot}(t) = \sum_{n=0}^{N} S_n(t) + \sum_{n<m} \left[S_{n,m}(t) + S_{n,m}^{\dagger}(-t)\right], \tag{2}$$

where $S_n(t) = A_n^2 s(t-\tau_n) \otimes s(t-\tau_n)$ are the autocorrelation of each signal involved and $S_{n,m}(t) = A_n A_m s(t-\tau_n) \otimes s(t-\tau_m)$ their cross-correlations. In terms of the original correlation function, it can trivially be shown that those two quantities reduce to [29]:

$$S_n(t) = A_n^2 S(t), \tag{3}$$

$$S_{n,m}(t) = A_n A_m S\big(t - (\tau_m - \tau_n)\big). \tag{4}$$

In case of planetary sounding, the amplitudes of the reflected signals might be very small ($A_n \ll 1$), in which case the main contributors to the final signal will be the incoming central autocorrelations peak S_0 and the cross-correlations of the reflected signals with the original one $S_{0,m}$.

B. Cross-correlation method

In the case of passive sounding through cross-correlation, the processing is similar to that of active sounding, although, instead of transmitting a signal, we measure the incoming signal (*e.g.*, the Jovian HOM/DAM radio signal) by switching on the receiver for a duration equal to that of the emitted signal in the active case. Let $s_{\text{ref}}(t)$ be the measured "incoming" signal, recorded for a duration T, and $r(t)$ be the "reflected" signal, recorded after a given time W_0 for a duration W_1 generally longer than T.

$s_{\text{ref}}(t)$ will contain both the incoming signal and the possible anterior reflections of that signal, whereas $r(t)$ will contain both the reflections of interest and the incoming signal:

$$s_{\text{ref}}(t) = \begin{cases} \sum_{n=0}^{N} A_n s_{\text{noise}}(t-\tau_n) & t \in [0, T], \\ 0 & \text{otherwise.} \end{cases} \tag{5}$$

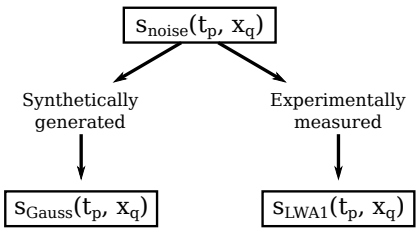

Fig. 1: The two types of time-dependence for the HOM/DAM radiation s_{noise} that will be considered in this study can be divided into two categories: synthetically-generated and experimentally-measured.

and

$$r(t) = \begin{cases} \sum_{n=0}^{N} A_n s_{\text{noise}}(t-\tau_n) & t \in [T+W_0, T+W_0+W_1], \\ 0 & \text{otherwise.} \end{cases} \tag{6}$$

While the two expressions make use of the same functions (incoming and reflected signals), they are of course taken at different instants in time. The cross correlation of the two,

$$R(t) = r(t) \otimes s_{\text{ref}}(t), \tag{7}$$

will reveal the possible features of the investigated body. In the case of a truly random external signal, there is no correlation between separated time segments such as $[0, T]$ and $[T+W_0, T+W_0+W_1]$. The only correlation will be between the incoming signal within $t \in [0, T]$ and the reflection of that signal within $[T+W_0, T+W_0+W_1]$, with the other terms simply raising background noise.

C. Noise datasets

Since processing is done on discrete signals, all time-domain signals considered in the simulations are digital signals, sampled at the sampling frequency f_s of the instrument. Moreover, the pulsed nature of a radar provides a discretisation of the along-track time, which is determined by the pulse repetition frequency (PRF) of the instrument. Thus, in our simulations, we consider that all external signals are discrete functions $s_{\text{noise}}(t_p, x_q)$ of the following sequences t_p and x_q:

$$t_p = t_0 + pT_s, \tag{8}$$

$$x_q = x_0 + qvT_a, \tag{9}$$

where $T_s = 1/f_s$ is the sampling period of the instrument, $T_a = (\text{PRF})^{-1}$ is the pulse repetition interval, and v the platform tangential velocity. t_0 and x_0 are the initial time and acquisition position of the radargram, respectively, and will be set to zero for our purposes.

Two types of signals will be considered to model external radiation throughout this paper: (i) synthetically-generated ones, in the form of band-limited Gaussian white noise s_{Gauss}, and (ii) experimentally-acquired waveforms of Jovian HOM/DAM, in the form of conditioned LWA1 data s_{LWA1}. This is schematically reported in Fig. 1.

1) White Gaussian noise: Let us consider a flat-spectrum band-limited Gaussian random noise of bandwidth B_b, duration T, and variance σ^2. It can be shown that the squared norm of its autocorrelation function is a cardinal sinus-like function with a peak of height $(2B_bT)^2\sigma^4$ and of width $1/B_b$, and with a constant background level at $2B_bT\sigma^4$, leading to a SNR of $2B_bT$ [1][2]. It can also be shown that such a signal is the most favourable for passive sounding, as any modulation in frequency will lead to spurious peaks.

In this study, the white noise signals $s_{\text{Gauss}}(t_p, x_q)$ are band-limited baseband complex-valued signals with the desired sampling frequency and PRF. The generation method of such signals is explained in Appendix A-A.

2) LWA1 measured noise: The LWA1 is a radio telescope composed of 256 bow-tie dipoles located in New Mexico, United States [11]. The DRX mode used in this study allows to collect the in-phase and quadrature components of 4-bit signal each (i.e. real and imaginary part of the complex waveform) from two orthogonal arrays at two tunings. Each tuning covers a total bandwidth of 19.6 MHz at an adjustable central frequency, totalling a frequency operating range from 10.2 to 88 MHz [10]. In this study, we use the array with the lower tuning, and limit the bandwidth to the 10.2 to 13 MHz range. These data are not calibrated, meaning that no absolute amplitude information is present in them. We use the default acquisition duration and PRF of 209 μs and 4785 Hz, respectively.

The conditioning of the raw data is explained in appendix A-B. The resulting signal $s_{\text{LWA1}}(t_p, x_q)$ is a baseband complex-valued signal with the desired sampling frequency and PRF.

III. Scattering equations

The simulation method used in the present study originates from the mutlilayer coherent radar echo simulator proposed in [14]. This method is based on the Stratton-Chu formula and the phase of each triangular facet of the DEM is computed through the linear phase approximation. A number of major modifications have been introduced in order to simulate passive and noisy active acquisitions, which are detailed in this section. The main changes pertain to the modelling of incoming fields, the treatment of time-dependant aspects, and the processing. The electric field $\mathbf{E_s}$ backscattered from a faceted surface is obtained through the reflection Stratton-Chu integral, whereas the subsurface field $\mathbf{E_t}$ is obtained through a transmission Stratton-Chu integral:

$$\mathbf{E_s}(t, \mathbf{r_r}) = ik_i \sum_\alpha \frac{E_i(\mathbf{r_\alpha}) s(t-\tau_\alpha)}{4\pi|\mathbf{r_r} - \mathbf{r_\alpha}|} \mathbf{F}_\alpha(\hat{\mathbf{k}}_\mathbf{i}, \hat{\mathbf{k}}_\mathbf{s}) \Phi_\alpha(\hat{\mathbf{k}}_\mathbf{i}, \hat{\mathbf{k}}_\mathbf{s}), \tag{10}$$

$$\mathbf{E_t}(t, \mathbf{r_r}) = -ik_t \sum_\alpha \frac{E_{\text{sub}}(\mathbf{r_\alpha}) s(t-\tau_\alpha^{\text{sub}})}{4\pi|\mathbf{r_r} - \mathbf{r_\alpha}|} \mathbf{F}_\alpha(\hat{\mathbf{k}}_\mathbf{i}^{\text{sub}}, \hat{\mathbf{k}}_\mathbf{t}) \Phi_\alpha^{\text{sub}}(\hat{\mathbf{k}}_\mathbf{i}^{\text{sub}}, \hat{\mathbf{k}}_\mathbf{t}). \tag{11}$$

In the above equations, $\mathbf{r_r}$ is the receiver position; $\mathbf{F}_\alpha$ is a vectorial quantity depending on the Fresnel coefficient and orientation of the facet, and on the backscattering geometry [19]; Φ_α is the phase contribution of the facet, computed according to the linear phase approximation [4]; τ_α and τ_α^{sub} are the delays with which the signals arrive back at the receiver, for a surface or subsurface reflector, respectively; lastly, $s(t)$ is the time-domain signal reflected by each facet, which takes different forms, depending on the sounding mode that we aim at simulating. In (10), $E_i(\mathbf{r_\alpha})$ is the amplitude of the incoming field at facet Δ_α, $\hat{\mathbf{k}}_\mathbf{i}$ the normalised incoming wavevector, and $\hat{\mathbf{k}}_\mathbf{s}$ the normalised scattering wavevector. In (11), $E_{\text{sub}}(\mathbf{r_\alpha})$ is the amplitude of the subsurface field arriving at surface facet Δ_α, $\hat{\mathbf{k}}_\mathbf{i}^{\text{sub}}$ is the normalised wavevector associated with that field, Φ_α^{sub} is the phase contribution of the considered facet, taking into account subsurface phase accumulation, and $\hat{\mathbf{k}}_\mathbf{t}$ is the normalised transmission wavevector, after refraction. For a given subsurface layer, $\hat{\mathbf{k}}_\mathbf{i}^{\text{sub}}$, $E_{\text{sub}}(\mathbf{r_\alpha})$, τ_α^{sub} and $\Phi_\alpha^{\text{sub}}(\hat{\mathbf{k}}_\mathbf{i}^{\text{sub}}, \hat{\mathbf{k}}_\mathbf{t})$ are computed through the iterative scheme described in [14]. The total received field $\mathbf{E_r}$ is given by the sum of the surface and subsurface fields:

$$\mathbf{E_r}(t, \mathbf{r_r}) = \mathbf{E_s}(t, \mathbf{r_r}) + \mathbf{E_t}(t, \mathbf{r_r}). \tag{12}$$

We neglect the curvature of the celestial bodies and consider that the orbiting platform travels at a constant altitude h and at a constant speed v. We set our system of coordinates so that the movement of the platform is aligned with the x-axis and centred along the y-axis. The position and the speed of the receiver at a given acquisition q is thus given by $\mathbf{r_r} = (x_q, 0, h)$, and its velocity vector, by $\mathbf{v_r} = (v, 0, 0)$. As the position of the receiver evolves only with x_q, we will denote it as $\mathbf{r_r}$ or x_q interchangeably, depending on the context. Doppler shift of received echoes are taken into account in the simulations presented in this paper (we remark that this feature was absent from the algorithm presented in [14] and represents an additional novel contribution to this paper); this is done through an appropriate modification of $s(t)$ in eq. (10) or (11), which is given in eqs. (17) and (21) for active and passive sounding, respectively.

We moreover assume that the antenna of the radar sounder is a half-wave dipole, with its axis being along the y-axis, that is, perpendicular to the direction of motion.

Figure 2 illustrates the acquisition geometry.

A. Active sounding

In active sounding with a single instrument, the configuration is monostatic. For every surface facet Δ_α, characterised by its incentre at a position $\mathbf{r_\alpha}$, the incident normalised wavevector $\hat{\mathbf{k}}_\mathbf{i}$ is given by

$$\hat{\mathbf{k}}_\mathbf{i} = \frac{\mathbf{r_\alpha} - \mathbf{r_r}}{|\mathbf{r_\alpha} - \mathbf{r_r}|}, \tag{13}$$

The backscattering vector in active monostatic sounding is simply the opposite of the incident wavevector :

$$\hat{\mathbf{k}}_\mathbf{s} = -\hat{\mathbf{k}}_\mathbf{i}. \tag{14}$$

Its emitted field $\mathbf{E_i}(\mathbf{r_\alpha})$ at any given surface facet incentre $\mathbf{r_\alpha}$ is given by

$$\mathbf{E_i}(\mathbf{r_\alpha}) = V_0 \frac{e^{ik_i|\mathbf{r_r} - \mathbf{r_\alpha}|}}{4\pi|\mathbf{r_r} - \mathbf{r_\alpha}|} \sin(\theta_\alpha) \hat{\mathbf{e}}_\mathbf{i}. \tag{15}$$

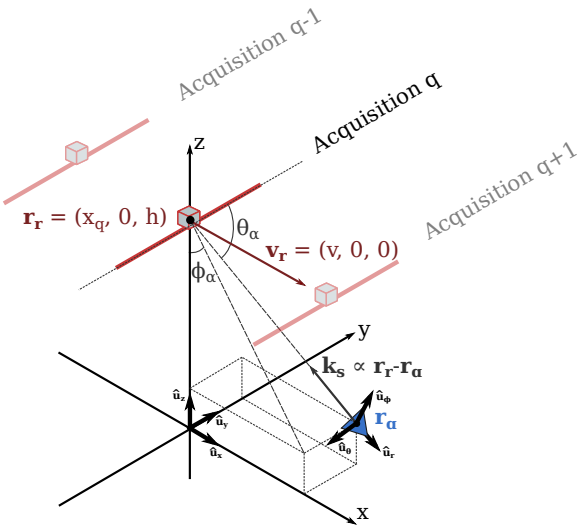

Fig. 2: Geometry of acquisitions.

V_0 is a characteristic of the instrument and therefore a known quantity: it is given by $V_0 = \sqrt{12\pi\eta_0 P}$ in terms of the total radiated power P, where $\eta_0 \approx 120\pi\ \Omega$ the vacuum impedance; or, alternatively, by $V_0 = k\eta_0 IL$ in terms of the current I flowing into the dipole antenna, where k is the wavenumber, and $L = \lambda/2$ the antenna length [12]. $\theta_\alpha = \arccos(\hat{\mathbf{u}}_\mathbf{y} \cdot \hat{\mathbf{k}}_\mathbf{s})$ is the angle between the dipole antenna axis and the coordinates of the facet incentre, as indicated in Fig. 2. The polarisation vector coincides with the polar angle unit vector $\hat{\mathbf{e}}_\mathbf{i} = \hat{\mathbf{u}}_\theta$, with the position of the spacecraft as reference point (the expression of this vector is given in cartesian coordinates in at equation (2) of [12]).

The emitted waveform is a Hann-windowed chirp of duration T:

$$s^{\text{ref}}_{\text{active}}(t) = W(t)\exp[i\pi B_w T^{-1}(t - T/2)^2], \qquad (16)$$

where $W(t)$ is the windowing function and B_w is the bandwidth of the chirp. This signal is in reality discrete, and sampled with a sampling frequency f_s. The time t is thus to be replaced by series (8). Taking the Doppler effect into account, the signal reflected from a given facet is $s_{\text{active}}(t_p - \tau_\alpha)$ or $s_{\text{active}}(t_p - \tau^{\text{sub}}_\alpha)$ where

$$\begin{aligned} s_{\text{active}}(t_p) = W(t_p)\exp\left\{i\pi\frac{B_w}{T}\left(t_p - \frac{T}{2}\right)^2\right\} \\ \cdot\exp\left\{2i\pi\frac{t_p}{\lambda}\mathbf{v_r}\cdot(\hat{\mathbf{k}}'_\mathbf{s} - \hat{\mathbf{k}}_\mathbf{i})\right\} \end{aligned} \qquad (17)$$

which is simply the emitted signal modulated by the Doppler phase factor. $\hat{\mathbf{k}}'_\mathbf{s}$ is the normalised backscattered wavevector from either the surface (in which case $\hat{\mathbf{k}}'_\mathbf{s} = -\hat{\mathbf{k}}_\mathbf{i}$ and the Doppler factor reduces to $\exp\{-4i\pi t_p\lambda^{-1}\mathbf{v_r}\cdot\hat{\mathbf{k}}_\mathbf{i}\}$), or the subsurface (in which case it is computed by the algorithm in [14]).

The field backscattered from the surface can be computed using the reflection Stratton-Chu formula in (10), using quantities defined in (13), (14), (15), and (17). The field reflected from subsurface layers is computed from (11); the initial wavevector and field of the recursion needed to determine the subsurface quantities (denoted with a *sub* index) are defined in (13) and (15), respectively.

B. Passive sounding

Due to the large distance that typically separates the source of external radiation (*e.g.*, Jupiter) from the target body (*e.g.*, its icy moons), and the comparatively short distance separating the spacecraft from the surface of its target, we assume that the external radio emissions propagate as plane waves in the space between the instrument and its target area. For our purposes, the incoming radiation is thus characterised by a constant wavevector $\mathbf{k}^\mathbf{J}_\mathbf{i}$. The surface backscattering vector, on the other hand is given by

$$\hat{\mathbf{k}}^\mathbf{J}_\mathbf{s} = -\frac{\mathbf{r_\alpha} - \mathbf{r_r}}{|\mathbf{r_\alpha} - \mathbf{r_r}|}, \qquad (18)$$

independently of $\hat{\mathbf{k}}^\mathbf{J}_\mathbf{i}$.

1) Incoming field: At any given point $\mathbf{r}$, the incoming field as described above is given by

$$\mathbf{E}^\mathbf{J}_\mathbf{i}(\mathbf{r}) = E^J_0 e^{i\mathbf{k}^\mathbf{J}_\mathbf{i}\cdot\mathbf{r}}\hat{\mathbf{e}}^\mathbf{J}_\mathbf{i}, \qquad (19)$$

where E^J_0 is the amplitude of the field, assumed constant due to the planar wave hypothesis, and $\hat{\mathbf{e}}^\mathbf{J}_\mathbf{i}$ its polarisation. This definition is valid up to a constant phase factor, which has no impact on the final backscattered intensity. The incoming wavevector depends on the geometry of the problem, and more specifically on the relative angle between the spacecraft – target body centre and the source – target body centre axes. For instance, $\hat{\mathbf{k}}^\mathbf{J}_\mathbf{i} = (0, 0, -1)$ describes the source of radiation being on the spacecraft zenith. The polarisation of the incoming wave should be chosen according to the characteristics of the type of radiation one wants to simulate. For example, auroral Jovian radiation is right-hand polarised, corresponding to $\hat{\mathbf{e}}^\mathbf{J}_\mathbf{i} = (1, -i, 0)/\sqrt{2}$ for a nadir-pointing wave. The field amplitude is determined as follows.

In the case of white Gaussian noise, the electric field amplitude can be derived considering that, for harmonic fields, the electromagnetic power radiated through a given area A is given by $P = \int_A \mathrm{d}\,\mathbf{A}\,(\mathbf{E}\times\mathbf{H}) = \frac{A}{2\eta_0}E^2$. This power can also be expressed in terms of the flux density S_J (in W/m^2/Hz) as $P = S_j A B_b$, where B_b is the noise bandwidth in Hz. By comparing those two expression we find

$$E^J_0 = \sqrt{2\eta_0 B_b S_J} \quad \text{(synthetically-generated)}. \qquad (20)$$

If $B_b > B_w$, the instrument bandwidth, then it is B_w which should be used in the equation above, since the instrument will not pick up on parts of the signal outside its own bandwidth.

In the case of LWA1 waveforms, the absolute amplitude information is disregarded in the analysis of the simulated data, since these data are not calibrated.

2) Time dependence: The time-dependence in passive simulations is implemented as follows. The external signal is already sampled at the sampling frequency of the instrument, either by design in the case of synthetically-generated white noise, either through interpolation in the case of

experimentally-measured signals. In the second case, the duration of the received signals is limited by the duration of the acquisitions (209 μs for LWA1 signals). Taking the Doppler effect into account, the signal reflected from a given facet in passive sounding is $s_{\text{passive}}(t_p - \tau_\alpha)$ or $s_{\text{passive}}(t_p - \tau_\alpha^{\text{ss}})$ where

$$s_{\text{passive}}(t_p) = \exp\left\{2i\pi \frac{t_p}{\lambda} \mathbf{v_r} \cdot \hat{\mathbf{k}}_\mathbf{s}^\mathbf{J}\right\} s_{\text{noise}}(t_p, x_q) \qquad (21)$$

where $s_{\text{noise}}(t_p, x_q)$ stands for either $s_{\text{Gauss}}(t_p, x_q)$ or $s_{\text{LWA1}}(t_p, x_q)$, as explained in sec. II-C.

3) Total backscattered field: The field backscattered from the surface can be computed using the reflection Stratton-Chu formula, given in (10), using $\hat{\mathbf{k}}_\mathbf{i}^\mathbf{J}$ as the incoming wavevector, (18) as the scattered wavevector, (19) as the incoming field, and (21) as the facet signal. The field reflected from subsurface layers is computed from (11), with the initial element of the recursion being $\hat{\mathbf{k}}_\mathbf{i}^\mathbf{J}$ for the surface wavevector and (19) for the surface field. It is worth noting that, since the incoming field shows no amplitude dependence with position, there is no spherical spreading of the incoming field, contrarily to the active case, where a inverse dependence in $|\mathbf{r_r} - \mathbf{r_\alpha}|$ applies.

As the reflected signal reaches the instrument, the receiver records both the reflected field $\mathbf{E_r}(\mathbf{r_r}, t)$ and the current incoming field. Due to the duration of the noise signals being inferior to the total duration of a typical radar acquisition (about 3000 μs in the case of RIME), we use the signal of the next acquisition to model the time-dependence of the incoming noise that arrives at the antenna when the backscattered signals reach it. The situation is schematically depicted in Fig. 3. Thus, the total received signal in the passive case is written as

$$\mathbf{E_r}(t_p, x_q) = \sum_\alpha \mathbf{E}_\alpha s_{\text{passive}}(t_p - \tau_\alpha, x_q) + \mathbf{E_i^{J'}}(t_p, x_{q+1}) \quad (22)$$

where $\mathbf{E}_\alpha$ is the time-independent field coming for a given facet, either surface of subsurface [*i.e.*, all factors of (10) or (11) except the $s(t)$ function], and $\mathbf{E_i^{J'}}(x_q, t_p)$ is the time-dependant Doppler-shifted incoming signal:

$$\mathbf{E_i^{J'}}(t_p, x_q) = \exp\left\{2i\pi \frac{t_p}{\lambda} \mathbf{v_r} \cdot \hat{\mathbf{k}}_\mathbf{i}^\mathbf{J}\right\} s_{\text{noise}}(t_p, x_q) \mathbf{E_i^J}. \quad (23)$$

The recorded incoming signal with which the field (22) should be cross-correlated is described in sec. IV.

C. Noisy active sounding

Due to the linearity of Maxwell's equations, the electric field collected during a noisy active acquisition in presence of an external field is given by the sum of the fields calculated in sec. III-A and III-B, which are the backscattered fields from active sounding signals, the fields backscattered from passive sounding signals and the incoming external fields. Since the active and passive simulations share the same characteristics (f_s, PRF, number of time-delay samples, number of acquisitions), we can simply add the two radargrams coherently.

IV. Signal acquisition and processing

The simulator generates raw sampled waveforms, which must be adequately post-processed to reveal the terrain features. In this work, we apply unfocused SAR processing to the data. This consists of range-compression, that is, an autocorrelation of the signal or a cross-correlation with a reference signal, and a coherent summation of range-lines over a length equal to the diameter of the first Fresnel zone. While this processing yields inferior SNR and SCR improvements compared to focused SAR processing, it requires less input parameters, and thus keeps our study more general.

The fields considered in the previous sections are all vectorial. When any field $\mathbf{E}$ arrives at the dipole antenna, the corresponding linear polarisation of the field is selected. This is the case for both passive and active acquisitions. Thus, the scalar electric field captured by the antenna is obtained by taking the dot product of any vectorial field in (10), (11), and (22) with the antenna polarisation $\hat{\mathbf{e}}_{\text{ant}}$. Schematically, we write:

$$\tilde{E}_r(t_p, x_q) = \sum_\alpha \mathbf{E}_\alpha(t_p, x_q) \cdot \hat{\mathbf{e}}_{\text{ant}} \qquad (24)$$

The thermal noise of the receiver has an energy of $k_B T$ joules, where $k_B \approx 1.38 \times 10^{-23}$ J/K is the Boltzmann constant and T the receiver temperature in kelvins. This contribution is negligible compared to the galactic background and Jovian noises in the HF-VHF band. The galactic has a spectral density of $k_B T_{\text{G}}(f_0)$ J/Hz, where the frequency-dependent galactic noise temperature at those bands is $\mathcal{O}(T_{\text{G}}) = 10^5 - 10^6$ K/Hz. When simulating with synthetically-generated Gaussian white noise, the amplitude of the noise can be set to any level, including that of the galactic background (*e.g.*, when Jovian emissions are at their weakest).

A. Noise-free and noisy active sounding

In the case of active sounding, regardless of the presence of the noise, the recorded signal is cross-correlated with the reference chirp signal to reveal features. The range-compressed radargram is thus computed as follows:

$$R_{\text{active}}(t_p, x_q) = \tilde{E}_r(t_p, x_q) \otimes_p s_{\text{active}}^{\text{ref}}(t_p), \qquad (25)$$

where the p subscript to the cross-correlation operator emphasises that the operation is carried out in the t_p domain.

B. Passive sounding

The reference signal in passive sounding contains the antenna polarisation vector component of both the Doppler-shifted incoming field (23) and that of anterior reflected fields, the computation of which has been detailed in sec. III-B. For a reason similar to the use of the $(q+1)$th acquisition in the incoming field of eq. (22), we use the reflected field from the $(q-1)$th acquisition to simulate the presence of anterior reflections in the reference signal:

$$E_{\text{passive}}^{\text{ref}}(t_p, x_q) = \mathbf{E_i^{J'}}(x_q, t_p) \cdot \hat{\mathbf{e}}_{\text{ant}} + \tilde{E}_r(t_p, x_{q-1}). \qquad (26)$$

This signal would be recorded during the time the radar instrument would normally emit the chirp. This duration T is typically smaller than the listening window W_1 of the instrument. To ensure that the peak of the cross-correlation function corresponds to the power reaching the antenna as in the active

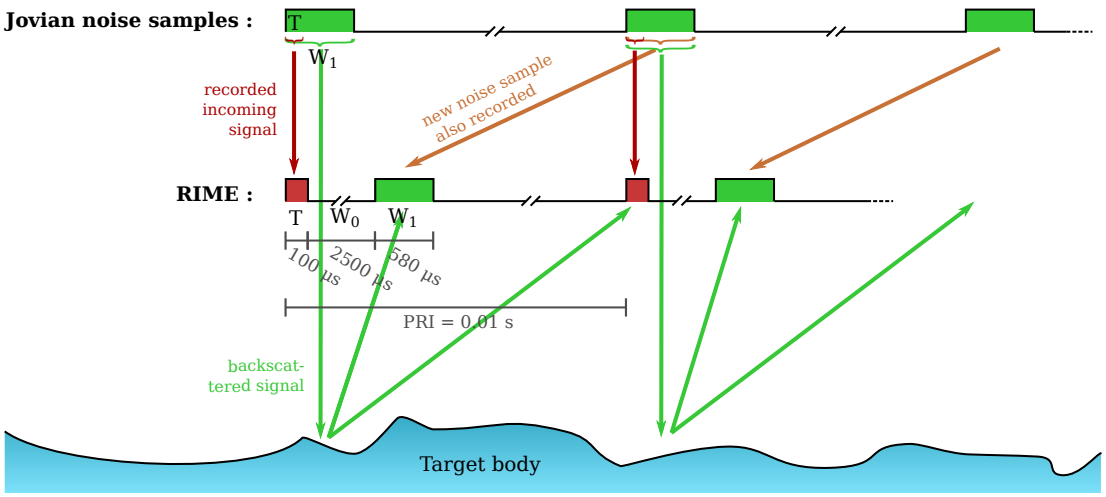

Fig. 3: Implementation of incoming and backscattered fields in simulations with a given sampled model of external (Jovian) noise, along with typical values for T, W_0 and W_1 for the RIME instrument.

case, we normalise the reference signal above by standard deviation σ of the signal (both synthetically-generated and experimentally-measured noise present a Gaussian distribution of amplitudes):

$$s^{\text{ref}}_{\text{passive}}(t_p, x_q) = \frac{1}{2\sigma} E^{\text{ref}}_{\text{passive}}(t_p, x_q). \tag{27}$$

The range-compressed signal is obtained by a cross-correlation of the first and second recorded signal:

$$R_{\text{passive}}(t_p, x_q) = \tilde{E}_r(t_p, x_q) \otimes_p s^{\text{ref}}_{\text{passive}}(t_p, x_q). \tag{28}$$

C. Unfocused SAR processing

Along-track direction processing is done by coherently stacking the range-lines located within one Fresnel zone of each other. This is valid for both passive, active in presence of external emissions, and noise-free active acquisitions. Let $\Delta = \lceil \sqrt{h\lambda/2} \cdot \text{PRF}/v \rceil$ be the number of samples covered by one Fresnel radius and $R(t_p, x_q)$ be a range-compressed radargram (actively or passively-acquired), we define $C(t_p, x_q) = \sum_{x'_q \in F(x_q)} R(t_p, x'_q)$, where $F(x_q) = \{x_{q-\Delta}, ..., x_{q+\Delta}\}$ is the set of acquisitions within one Fresnel zone of x_q.

D. Signal power

The final step is to represent the radargram in physically-meaningful units of power (W). For any type of data $B(t_p, x_q)$, which can represent both range-compressed or SAR-focused data (either in active or passive mode), the power radargram will be given by $P(t_p, x_q) = \frac{A_{\text{eff}}}{2\eta_0} \|B(t_p, x_q)\|^2$ where $A_{\text{eff}} = 1.67\lambda^2/4\pi$ is the effective area of the dipole antenna. The norm is understood to be an element-wise norm.

V. Validation

Since the noise-free active monostatic simulation method upon which the proposed simulator has been developed was already thoroughly validated [14], we focus in this section on aspects related to noisy active sounding, passive sounding, and to processing, which are new. We also provide a more in-depth analysis of the absolute power levels in both sounding modes.

TABLE I: Main characteristics of the RIME instrument used throughout the paper.

Transmitted power	P	10 W
Central frequency	f_c	9 MHz
Bandwidth	B_w	2.8 MHz
Sampling frequency	f_s	12 MHz
Transmit window	T	100 μs

In our validation test case, we will consider band-limited Gaussian flat-spectrum noise, which allows us to compare our results with the analytical results found in the literature. The radar instrument shares the characteristics of RIME, which are summarised in table I. Its altitude is set at $h = 400$ km, its orbital velocity at $v = 1806$ m/s, and its PRF at 100 Hz. The listening window is set to $W_1 = 580$ μs. The incoming noise is characterised by $\hat{\mathbf{k}}^{\mathbf{J}}_{\mathbf{i}} = (0, 0, -1)$ and by $\hat{\mathbf{e}}^{\mathbf{J}}_{\mathbf{i}} = (1, i, 0)/\sqrt{2}$.

A. Flat layers: comparison with radar equation

We compare the signals obtained with passive and noisy active acquisition modes for flux densities ranging from $S_J = 10^{-19}$ to 10^{-15} W/m^2/Hz between themselves and with the theoretical results obtained through the radar equation. The terrain is modelled with two perfectly smooth layers[1] separated by a distance of 1460m, the surface has a dielectric constant of $3 + i0.001$ and the subsurface a dielectric constant of 5. With those dielectric constants, we can predict the subsurface echo to stand at about 8.5 dB below the surface echo. The simulation footprint is limited to the the first Fresnel zone of the radar.

One thousand range-lines were simulated. The signals that we present in this section are average power levels for a given processing. The backscattered power in the noise-free active case is -99.5 dBW before any processing is applied, which

[1]To minimise artefacts such as Bragg resonances, we add a negligible but non-zero amount of roughness ($< \lambda/30$) whenever simulating otherwise "perfect" geometrical shapes.

is in agreement with the -100 dBW obtained using the radar equation.

The noisy active simulations with unfocussed SAR processing are shown in Fig. 4. The results are in agreement with the radar equation [31] both in terms of the absolute post-processing backscattered power and signal-to-noise ratio (SNR). Specifically, the peak power obtained with the proposed technique is -3.6 dBW (-1.8 dBW according to the radar equation) and the SNR 53.7 dB in the $S_J = 10^{-19}$ W/m^2/Hz (55.1 dB according to the radar equation). As expected, the noise background raises by 10 dBW every time the noise flux density is increased by a factor of 10. The subsurface peak is located at 16.92 μs from the surface, which exactly corresponds to the two-way travel time of light over the interlayer distance, and its power stands at 8.5 dB below the surface power, which is in agreement with expectations.

The simulated passive sounding radargrams are shown in Fig. 5. Since the reference literature considers autocorrelation of the signals, we present the autocorrelated waveforms with no further processing (unlike the more slightly complex cross-correlation method described in sec. IV-B), but with the same normalisation as in (27). In order to visualise the self-power peak of (3), we used $\mathbf{E_i^{J'}}(x_q, t_p)$ as the second term of (22). Seven signals can be identified: the central autocorrelation peak, corresponding to S_0 in (3), the surface peak S_1 at -231.9 μs and its symmetric, the subsurface peak S_2 at -215 μs and its symmetric, and the faint cross-correlation peak $S_{1,2}$ in (4) at 16.92 μs and its symmetric[2]. The peak-to-background ratio remains constant for every flux S_J at about 34 dB, which is in agreement with the theoretical value of $10\log(2B_wT_s) = 35.1$ dB. Absolute power levels can be compared to the equations of [1]. The squared amplitude of the peak is given by $2B_wT_s\sigma^4$ for an autocorrelated signal. Here we are computing the power of an electric field captured by an antenna, cross-correlated with a normalised copy of itself. The expected peak power is thus given by $\frac{A_{\text{eff}}}{\eta_0}B_wT_s\sigma^2$, which is -33.6 dBW for $S_J = 10^{-19}$ W/m^2/Hz. The value of -32.5 dBW obtained with the proposed simulator is thus in agreement with theory. The peak S_1 coming from the surface echo stands 12.6 dB below the self-power peak for all fluxes. This is again in agreement with the theory, as the Fresnel's coefficient of ice leads to a loss $10\log(R^2_{\text{srf-vac}}) = -11.4$ dB (the incoming planes waves encounter no losses due to geometrical spreading when reflecting on a perfectly flat surface). The subsurface peak can be observed 16.92 μs from the surface and stands 8.2 dB lower, as expected. When the noise flux density is increased, the entire signal gains power but SNR is conserved, as expected.

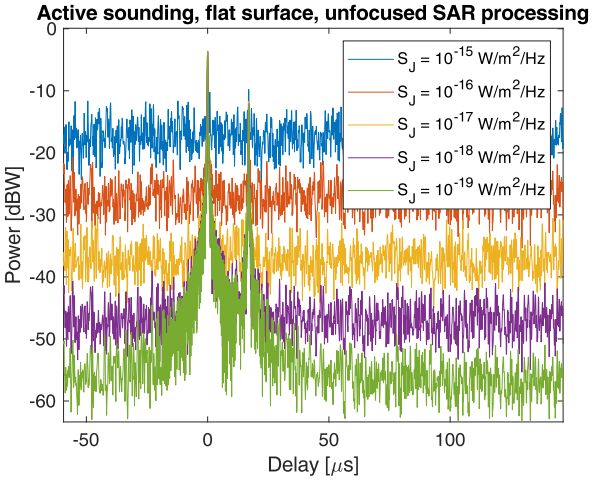

Fig. 4: Average A-scan for incoming noise flux densities of 10^{-19} to 10^{-15} W/m^2/Hz for the validations scenario described in the text, using active sounding and unfocused SAR processing (the zero-delay point is off-centred for readability).

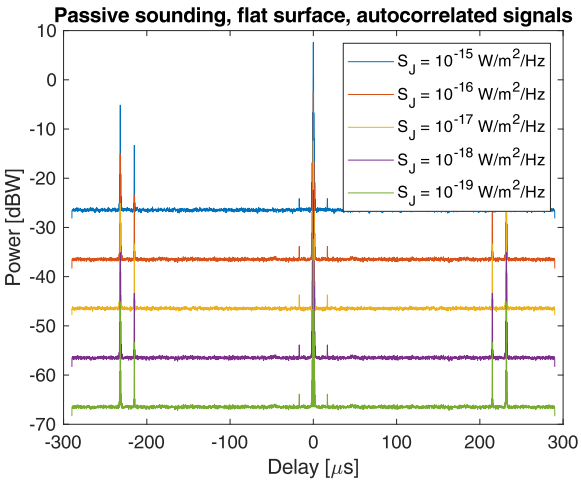

Fig. 5: Average A-scan for incoming noise flux densities of 10^{-19} to 10^{-15} W/m^2/Hz for the validations scenario described in the text, using passive sounding and the autocorrelated signals.

B. Rough surface: comparison with geometrical spreading factor

Now that we have established a near-perfect agreement of peak echo power with the radar equation on flat layers, we analyze the peak power backscattered from a rough surface relative to the peak power backscattered from a smooth surface. In other words, if P_0^s is the surface absolute power level obtained with a flat layer, and P^s that obtained with a rough surface, we are interested in the P^s/P_0^s ratio. For surface echoes, a "geometrical spreading factor" was derived for both active and passive sounding in [31], which is based on the idea that backscattered waveforms experience a spreading with an angle equal to the rms slope of the scattering surface σ_s. Although approximate, it provides a useful benchmark against which to compare the results of the proposed simulator.

[2]In this test, we let the delay of the signals fold as many times as needed in order to fit into the 580 μs window without correcting for it. Only the relative delay of the subsurface with respect to the surface has a meaning, and has indeed the correct value.

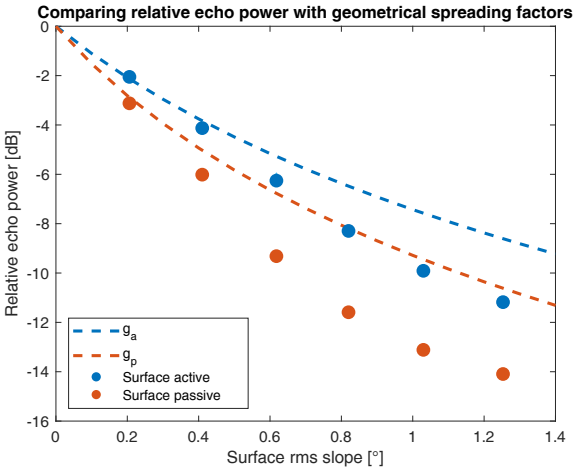

Fig. 6: Surface peak power versus surface roughness (expressed with surface rms slope [°]), relative to a simulation with a flat layer. The surface data points for active and passive modes are represented as blue and orange dots, respectively. As a reference, the active and passive spreading factors g_a and g_p are shown as blue and orange dashed lines, respectively.

The factors for active and passive sounding are, respectively,

$$g_a = \lambda^3 (8\pi h)^{-1} \left\{ \sqrt{\frac{h\lambda}{2}} + h \tan\left[\arctan\left(\sqrt{\frac{\lambda}{2h}} + \sigma_s \right) \right] \right\}^{-2}, \quad (29)$$

$$g_p = \left[1 + \sqrt{\frac{h}{\lambda}} \tan(\sigma_s) \right]^{-2}. \quad (30)$$

Since there are no literature studies for the power of echoes from rough subsurface layers, we decided not to include any subsurface features in the DEMs of this validation test. The dielectric constants of the surface are identical in all DEMs. The rough surface DEMs have an rms slope of $\sigma_s = 0.21, 0.41, 0.62, 0.82, 1.03$ and 1.25 degrees. Higher roughness levels were not analyzed because of the short autocorrelation time of passive signals ($580\mu s$), which prevents the detection of echoes if these are too weak.

The results are shown in Fig. 6. The spreading factor of active signals (blue dashed line) decays slower than that of passive signals (orange dashed line). This tendency is also observed with the relative surface echo power obtained by the proposed simulator (blue and orange dots), although the decay is faster for both active and passive modes. Some level of discrepancy is expected since we compare a formula depending simply on λ, h, and σ_s, and simulations involving the full phase and polarimetry information of backscattered signals. Given these differences, we consider the fact that we observe the same dynamics to be a satisfactory result.

C. Rough multilayer terrain: cross-correlation window length

In the previous sections, we probed the response of the proposed simulator for active and passive sounding using autocorrelated signals in the latter. In this section, we explore the behaviour of the simulator for cross-correlated signals, making rigorous use of the equations presented in sections III and IV, and with a random rough target area. The goal is to test the properties of simulated passive signals for various listening windows T in a more realistic scenario. The later listening window W_1 is still fixed to 580 μs. A Hann window was also applied to the chirp in the active case.

The terrain now comprises a random rough surface with a dielectric constant of $3+i0.001$ and a random rough subsurface with a dielectric constant of 15, located at an average depth of 1460m. The facet length is $\Delta_X = 500$ m. Both were procedurally-generated through a fractional Brownian motion (fBm) process with a Hurts' coefficient $H = 0.65$ and an root mean square (rms) height difference at resolution scale of $\sigma_0(\Delta_X) = 12.35$ m. The DEM, crossed from left to right, is shown in Fig. 7. We fix the noise flux at 10^{-18} W/m^2/Hz, that is, ten times higher than the galactic background.

For context, the complete radargrams (power and phase) after range-compression for noise-free active, noisy active and passive sounding mode is shown in Fig. 8. On Fig. 9, the incoherently average of all range-compressed range lines are shown for both active and passive sounding. Different values of the incoming listening window $T = 50$, 100, 250, 550 μs are considered in the passive case. As expected, when the initial listening window is increased, the noise floor and the peak increase by different amounts in a way that increases the SNR. The subsurface signal appears above the background on the signals with $T = 250$ μs and 550 μs around the expected average optical depth of $\sqrt{3} \cdot 1460\text{m} \approx 2500\text{m}$. The overall low absolute power and SNR values in either mode is not surprising given (i) the high terrain roughness, (ii) the choice of an "intermediate" value of the flux density, and (iii) the fact that only range-compression is applied to the signals.

Comparing the active and passive average rangelines, we can see that, while surface echoes are roughly similar in shape, subsurface echoes appear more clearly in active sounding. We believe this effect to be the subsurface equivalent of the fact that passive signals undergo stronger geometrical spreading that active ones (see sec. V-B and ref. [31]). Nevertheless, since there is no literature on subsurface passive sounding of rough interfaces, a detailed quantitative explanation of this effect falls outside the scope of this paper, which is focused on describing a simulation algorithm. Thus we defer the study of passive subsurface signals to a later work.

Note that lack of previous literature on passive subsurface radar sounding makes it difficult to quantitatively validate all the components of the the simulation method in detail in this more realistic case. However, the satisfying response we obtained in all tested situations provides evidence of the proper behaviour of the simulator.

VI. Simulations with Jovian waveforms

In this section, we present simulation results on terrains which we believe are representative of selected areas of Europa and Ganymede, and using experimentally-acquired samples of the Jovian noise. Due to the scarcity of quality DEMs of the Jovian icy moons, we resorted to using 200 and 500m-resolution martian DEMs of "analogue" areas of given targets

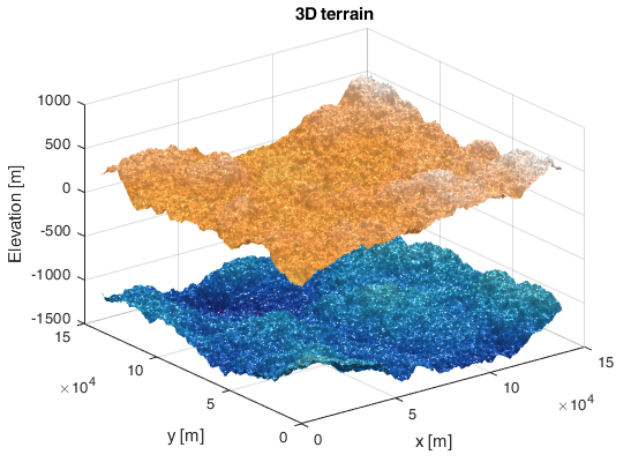

Fig. 7: Digital terrain model used in the simulations for the rough multilayer validation test described in sec. V-C (axes not to scale).

on the icy moons [13]. We note that the current simulator does not model roughness below DEM scale, which, in the case of icy moons, may lead to non-negligible coherent losses.

The radar instrument shares the characteristics of RIME, which are given in table I. The incoming noise is characterised by $\hat{\mathbf{k}}_\mathbf{i}^\mathbf{J} = (0, 0, -1)$ and by $\hat{\mathbf{e}}_\mathbf{i}^\mathbf{J} = (1, i, 0)/\sqrt{2}$.

A. Jovian DAM samples

For each terrain, two signals in total are used: a synthetically-generated one, and a LWA1 one.

Simulations with band-limited flat-spectrum Gaussian noise with a power flux density $S_J = 10^{-16}$ W/m^2/Hz are used as reference in all cases.[3] For the "Ganymede" simulation, we used LWA1 signals recorded on the 27/03/2017 between 11:50:30 and 11:51:30. For the "Europa" simulation, we used a LWA1 acquisition from the same day, collected between 08:54:37 and 08:54:46. The spectra and corresponding auto-correlation functions of all these acquisitions are shown in Fig. 11 for the "Ganymede" simulation, and in Fig. 12 for the "Europa" simulation.

The LWA1 signals used for the "Ganymede" simulation show an Io-C event including emissions changing from millisecond to second scales. The LWA1 signals used in the "Europa" simulation display an Io-A event which exhibits only smooth emissions varying on time scales of the order of the second. They are both affected, to some extent, by Faraday fringes, interplanetary scintillation, and modulation lanes. The slow periodic fluctuations observed in these data are thought to come at least partially from interplanetary scintillation, which may therefore also be present in RIME acquisitions. Faraday fringes generate a ghost echo in the the autocorrelations, which will have to be ignored in the interpretation of the data.

[3]The flux is predicted to be higher on Europa than on Ganymede. However, setting the flux to the same value for both simulated terrains will allow an easier comparison between them.

B. Ganymede simulation

The "Ganymede" simulation was carried out on a DEM of the chaotic terrain south of Lycus Sulcus, surrounding Olympus Mons. This terrain is extremely rough from a radar point of view, and has been considered comparable to the rough bright terrain of Ganymede [3]. The DEM we used contains a smoother part on the left and a rougher part on the right. The dielectric constant was set to 5. To conduct a realistic experiment, the PRF of the instrument was set to 200 Hz and its altitude to 500 km, in accordance with the current mission design for RIME operations on Ganymede [35]. The simulated track is about 107 km long and contains about 12 000 rangelines. Fig. 10-(a) shows the trajectory superimposed on a map of the DEM.

The results are shown in Fig. 13. The noise-free active simulation result, shown in Fig. 13-(a), confirms that the considered terrain is very rough. Indeed, the radargram is dominated by clutter generated from the many crevasses of the DEM, and a linear, surface-like feature can only be seen on the left half of the radargram. The absolute power is also quite low. The noisy active simulations with flat-spectrum noise is shown on Figs. 13-(b).[4] We can see that the Jovian emissions completely overpower the surface echo, off-nadir and nadir alike. This is not surprising given the high roughness of the terrain and the high density fluxes of both signals. The passive simulation result obtained with the LWA1 waveforms is shown on Fig. 13-(c). Here the surface can be seen in a satisfactory way on the areas where the surface is smooth, around the first 30 kilometres, and where the signal is strong, such as between 90 and 100 km. Fig. 13-(d) shows a simulation carried out with white noise over a duration of 200 μs. Some differences between Fig. 13-(c) and (d) can be seen, highlighting the effect of the non-whiteness of actual Jovian emissions. These differences pertain to slow along-track amplitude variations (*e.g.*, kilometres 90-100), and relative strength of nadir versus off-nadir echoes (*e.g.*, kilometres 10-30).

C. Europa simulation

In the "Europa" simulation, the target area was modelled with two layers, which represent the icy surface and the ice-ocean interface. The terrain resolution is set to $\Delta_X = 500$ m for both layers. The surface comes from a DEM of the fault system of Tempe Terra, Mars, which is characterized by long linear depressions, whereas the subsurface was procedurally-generated through a fBm process with a Hurst's coefficient of $H = 0.89$ and a rms height difference at resolution scale of $\sigma_0(\Delta_X) = 1.1$ m. The DEMs for both layers can be seen in Fig. 10-(b). The subsurface depth varies between 8.5 and 9 km from the average altitude of the surface. Europa presents significant small-scale roughness [24], which is neglected in these DEMs. The dielectric constants of the surface and subsurface were set to be $\epsilon_1 = 2.95 + i0.00295$ and $\epsilon_2 = 80$, respectively. The attenuation is higher than what was modelled in previous studies [15], but since our simulator does not currently model volume scattering and small-scale roughness

[4]Since the LWA1 signals do not possess absolute amplitude information, it did not make sense to include their noisy active result.

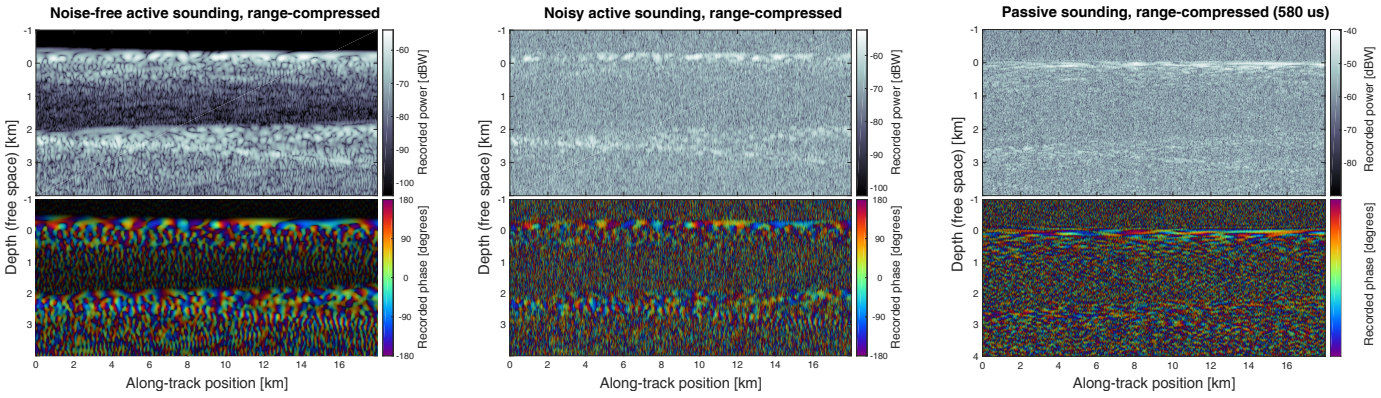

(a) (b) (c)

Fig. 8: Simulated radargrams for the terrain model shown in Fig. 7 with a RIME-like instrument, for (a) noise-free active, (b) noisy active, and (c) passive sounding, assuming a flux of 10^{-18} W/m^2/Hz. For each acquisition mode, the power collected by the antenna is shown (in dBW) on the top, and the phase of that signal (in degrees) on the bottom.

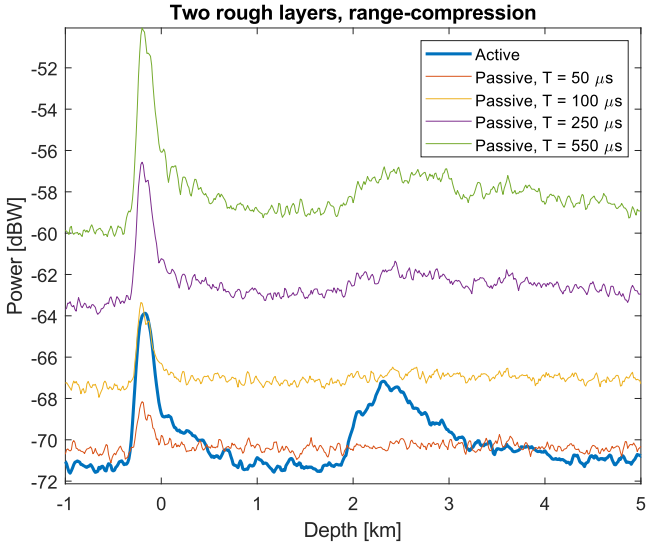

Fig. 9: Incoherently-averaged rangelines of the simulations shown in Fig. 8 for active sounding and for passive sounding using different incoming noise listening windows.

coherence losses, we settled on choosing a slightly stronger attenuation to compensate. In these simulations, the PRF of the instrument was set to 400 Hz, and the altitude to 400 km, which is in line with the current RIME plan of operations for Europa flybys [35]. The total track contains about 2500 rangelines and spans about 20 kilometres.

Fig. 14 shows the obtained results. Fig. 14-(a) displays the noise-free active simulation, where the surface and the subsurface layer can easily be identified, although some clutter from the crevasses is present. The oceans echo stands at about 15.5 km below the surface and has an intensity that is 12 dB lower. Fig. 14-(b) displays the results of simulations of active acquisitions obtained considering synthetic waveforms as incoming waveform. Predictably, none of the echoes can be unambiguously identified, although the bright streak around 0 km altitude can be identified as the surface. The passive simulation results obtained with the LWA1 waveforms and white noise signals of the same duration are shown in Fig. 14-(c) and (d), respectively. With this DEM, the surface echo can easily be seen in almost all cases, although the subsurface is very difficult to distinguish. On the passive LWA1 simulation, a brighter zone appears between kilometres 11 and 17. This brief surge of power can also be seen in the original spectra and autocorrelation function of the Jovian signal (see Fig. 12), and is being propagated across a larger distance by the unfocused SAR processing. The impact of such an effect on the visual quality of the radargram could be mitigated by using adequate signal processing techniques (which are outside the scope of this paper). Apart from this feature, Figs. 14-(c) and (d) do not show significant differences, which is expected, since the spectrum of the LWA1 acquisition is rather flat.

D. Discussion

In the previous subsections we have shown how the surface and the subsurface of terrains representative of Ganymede and Europa would appear as seen by a RIME-like instrument in a standard noise-free active mode, noisy active mode, and passive mode. These examples, in complement to the results of Sec. V, illustrate the flexibility of the simulator in generating radargrams under these three acquisition modes, in a coherent and comparable way.

Without any surprise, noiseless active sounding is by far the most favourable setting. However, in the presence Gaussian white noise with $S_J = 10^{-16}$ W/m^2/Hz, active sounding hardly reveals any feature for the two modelled target areas. The simulated examples show how passive sounding is able to retrieve the surface of both the "Ganymede" and "Europa" terrain, even in the case of very high roughness. The subsurface of the “Europa” terrain could, on the other hand, only be seen in the noiseless active sounding simulation.

The simulations also visually highlight the differences that can arise from the non-whiteness of Jovian emissions, although, for the examples tested, these differences did not endanger the visibility of features of interest in either radargrams.

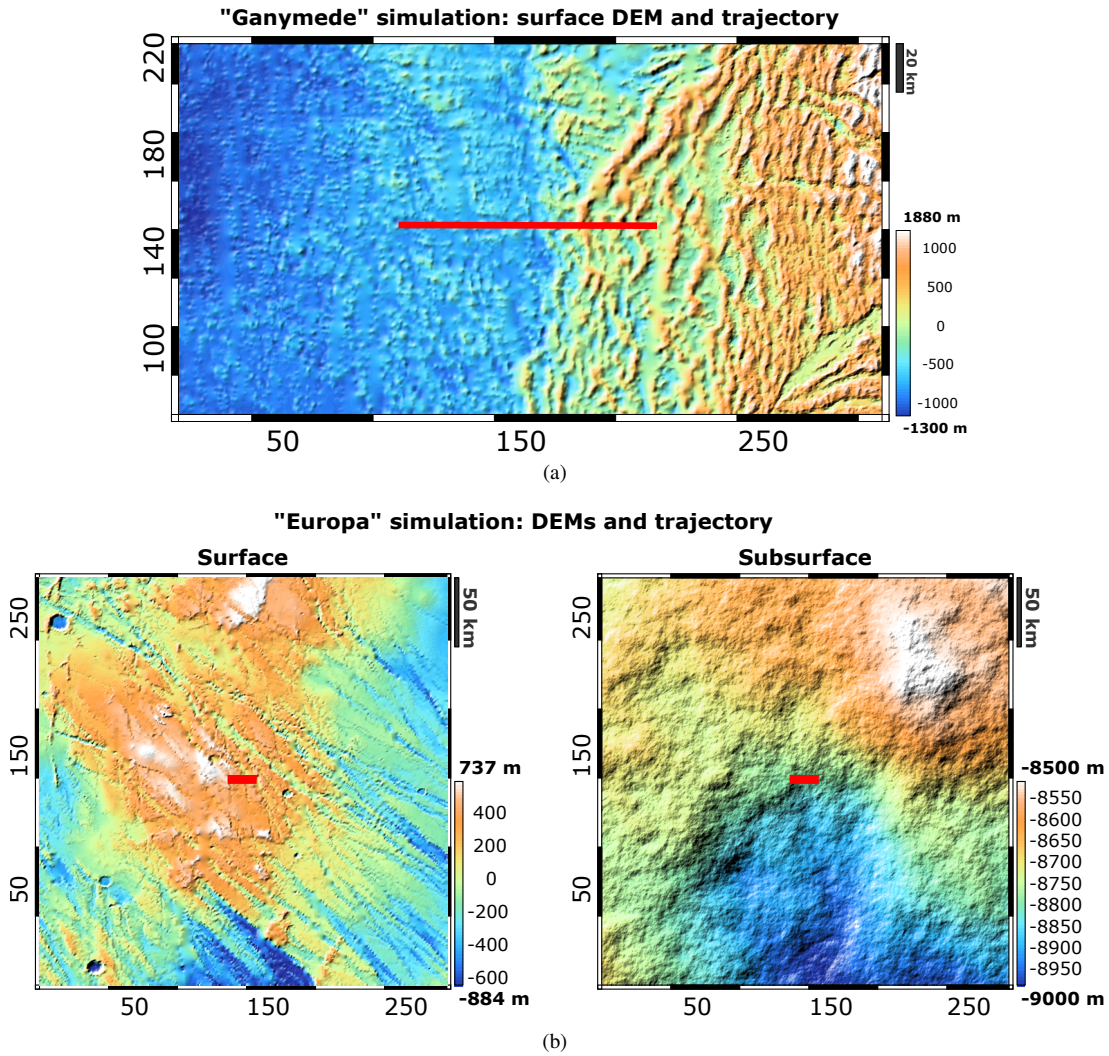

Fig. 10: (a) Coloured hill-shade elevation map of the surface DEM used in the "Ganymede" simulation, which is coming from the chaotic terrain surrounding Olympus Mons, Mars. (b) Coloured hill-shade elevation maps of the DEMs of the surface and subsurface used in the "Europa" simulation; the surface represents an area of Tempe Terra, Mars, whereas the subsurface is procedurally-generated with a fBm process. The spacecraft trajectory during the acquisition is shown as the thick red line superimposed over all maps.

VII. Conclusion

We presented a technique for simulating passive and active radar acquisitions in presence of external radiation, which is based on the Stratton-Chu formula used alongside the linear phase approximation on triangular facets. The proposed simulator takes into account all main instrument parameters, simulates the Doppler effect, and can produce raw, range-compressed, or unfocused SAR-processed radargrams. It is able to compare active and passive acquisitions under otherwise identical conditions. The validation of the proposed simulator is challenging due to the fact that passive sounding has never been tried with an existing orbital radar sounder, meaning that no real-life data against which we could compare our simulations exist. The literature is also devoid simulated passively-acquired radargrams, which could also be used as benchmarks. Thus the only way to have a quantitative validation is to compare our results with analytical formulas based on the radar equation. Despite the important differences that exist between such first-order formulas and a coherent simulator including time-domain processing, we were able to reach good agreement with the results from earlier studies in controlled setups.

In order to show examples of how the proposed simulator could be used to support planned Jovian radar missions, we applied our method to the case of radar sounding of the Jovian icy moons Ganymede and Europa. We considered waveforms of the Jovian decametric radio emissions that were measured from Earth, and modelled the other electromagnetic aspects of the Jovian emissions according to the literature. Using digital elevation models from analogue areas of Mars, we produced simulated radargrams in active and passive mode. We finally presented a qualitative comparison of the two for both analogue terrains.

Our study suffers from a number of limitations. Regarding

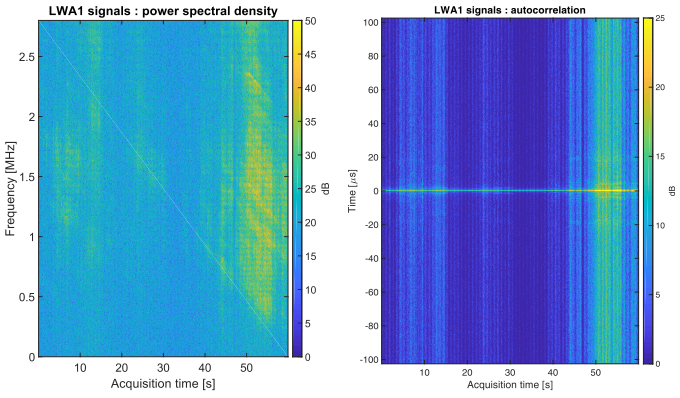

(a) (b)

Fig. 11: LWA1 waveforms used in the "Ganymede" simulation: (a) spectral density, (b) autocorrelation.

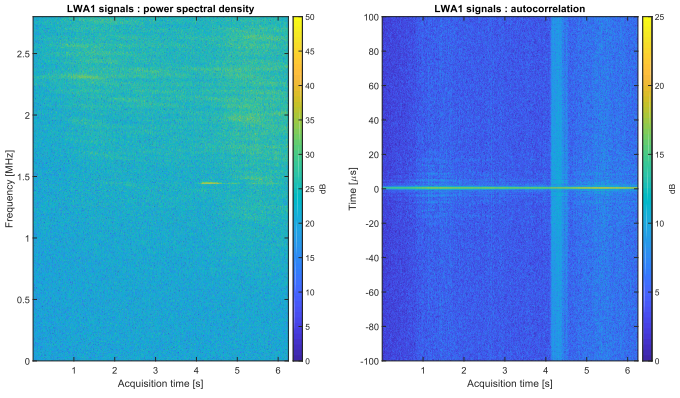

(a) (b)

Fig. 12: LWA1 waveforms used in the "Europa" simulation: (a) spectral density, (b) autocorrelation.

the simulation algorithm itself, the greatest caveat is the lack of a small-scale roughness in the DEM electromagnetic response. There are currently no DEMs of planetary bodies with a resolution sufficient to fully model scattering ($\lesssim \lambda/10$) at typical radar sounder wavelengths. While we can comfortably simulate on DEMs with resolutions as low as hundred of metres with the linear phase approximation, these do not contain information about small-scale roughness, and thus part of the scattering process is neglected. On the side of Jovian simulations, the main factors limiting the impact of the presented examples are : (i) the lack of DEMs of the Jovian moons that span sufficiently large areas with a high enough resolution, and (ii) the lack of high-resolution, calibrated and interference-free waveforms of the Jovian HOM/DAM from space. Thus, despite the examples of application of the proposed simulator to the RIME case providing interesting results for confirming the value of the simulation technique, they cannot be used for drawing more ascertained conclusions regarding the relative value of active and passive sounding on the Jovian icy moons.

In our simulations, we neglected parts of the acquisition chain of a real radar instrument, notably the quantisation of the received signals. However, we do not believe this has a significant effect, since we were able to obtain very satisfactory results (as far as spectral content is concerned) with the 4-bit resolution signals from the LWA1 radio telescope. The presence of ionosphere was also neglected. On the Jovian icy moons, Faraday rotation might affect the linear polarisation of the active signals and the elliptically-polarised Jovian signals in different ways. We consider that investigating the issue in the passive case is outside the scope of this article, although we note several algorithms exist to correct ionosphere phase distortion in the active case [23][30]. We also note that the quality of passively-acquired radargrams maybe be improved with appropriate processing techniques, such as cross-correlation that would omit a given set of strong narrow-band emissions.

The rough phase response of a facet, which would allow simulation of small-scale roughness, is the subject of ongoing research. Future work will also consider more precise simulations based on actual Europa or Ganymede DEMs, with a rough facet phase formulation, and with high-quality samples of the Jovian emissions (or a model thereof). Such waveforms could consist of a synthetically-generated stochastic part and a "structural" component of experimental measurements, all at the right PRF and sampling frequency. The simulator could also be used to study radar sounding on other bodies where passive sounding could have scientific added value, such as Enceladus using Saturn's emissions, or the Moon with terrestrial auroral kilometric radiation, provided sufficient data exists to model these emissions. Other future work might include the use of the simulator to investigate the properties of subsurface passive signals.

ACKNOWLEDGMENTS

This work was supported by the Italian Space Agency through "Attività scientifiche per JUICE fase C/D" under Contract ASI/INAF n. 2018-25-HH.0. The research at the University of Iowa was supported by NASA through Contract 699041X with the Southwest Research Institute. The authors would like to thank Baptiste Cecconi and Cyril Grima for exchanging ideas. Part of the data used in this paper have been collected by the LWA1, the construction of which has been supported by the Office of Naval Research under Contract N00014-07-C-0147. Support for operations and continuing development of the LWA1 is provided by the National Science Foundation under grants AST-1139963 and AST-1139974 of the University Radio Observatory program.

APPENDIX A
GENERATION/CONDITIONING OF NOISE SIGNALS

Two types of signals were used to model the Jovian emissions throughout this study: synthetically-generated white noise s_{Gauss} and conditioned LWA1 data s_{LWA1}. In this appendix, we provide the details of the generation/conditioning methods applied to obtain them.

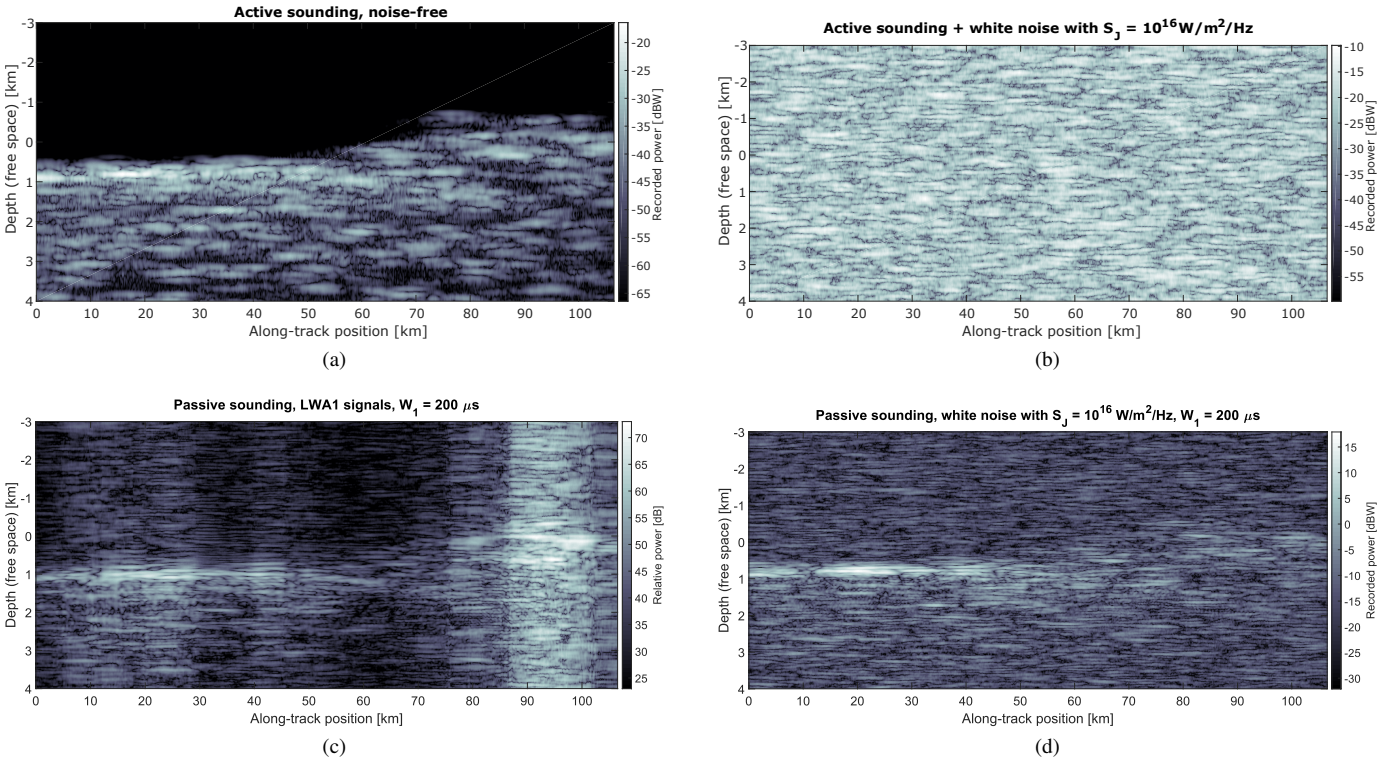

Fig. 13: Simulation results for the Ganymede simulations. (a) Noise-free active, (b) active in presence of Jovian noise modelled with synthetically-generated Gaussian noise, (c) passive simulation based on the LWA1 signals shown in Fig. 11, (d) passive simulation using white noise of comparable duration.

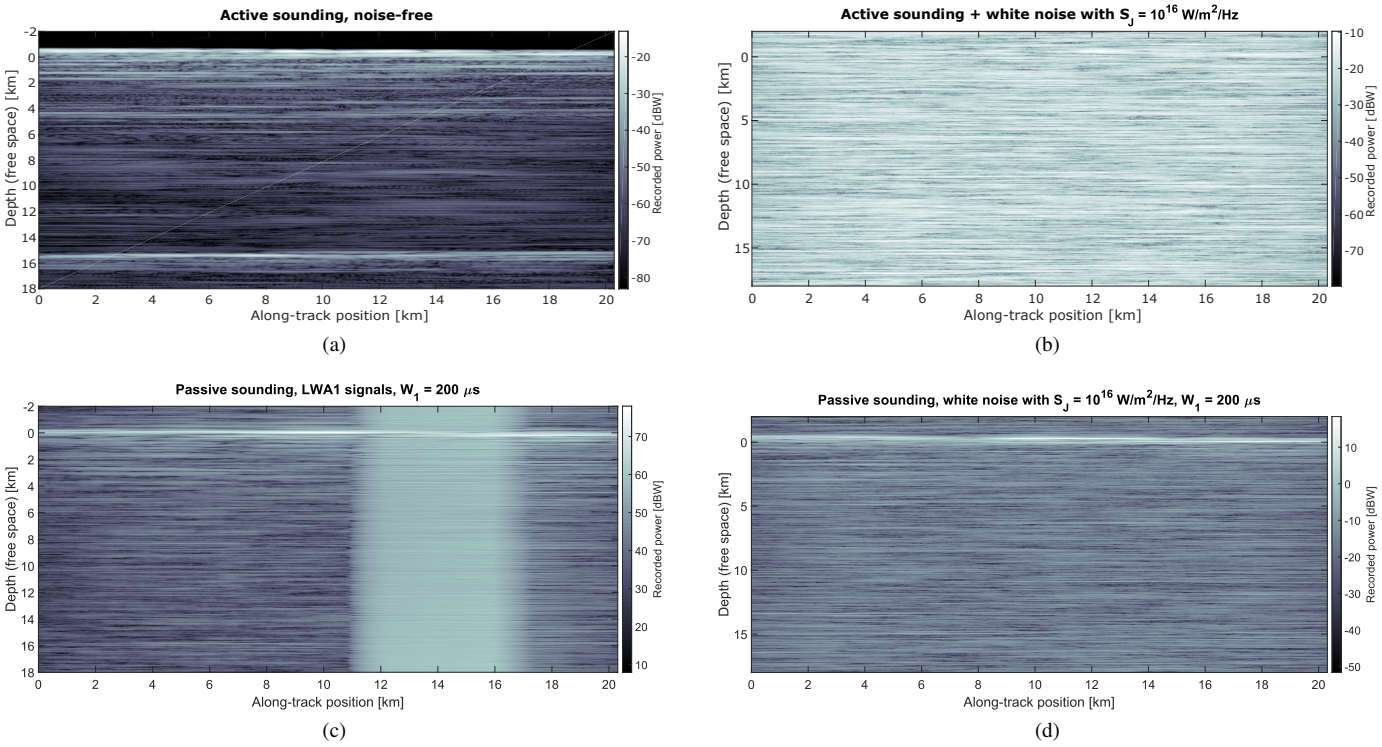

Fig. 14: Simulation results for the Europa simulations. (a) Noise-free active, (b) active in presence of Jovian noise modelled with synthetically-generated Gaussian noise, (c) passive simulation based on the LWA1 signals shown in Fig. 12, (d) passive simulation using white noise of comparable duration.

A. Gaussian band-limited flat-spectrum noise

The Gaussian noise signals that we consider in the simulations are generated in two steps. The first step is the generation of an array of uncorrelated random complex numbers, with both the real and the imaginary part following normal distributions:

$$s_{\text{Gauss}}(t_p, x_q) = \frac{1}{\sqrt{2}}[s_{\text{Gauss;1}}(t_p, x_q) + i s_{\text{Gauss;2}}(t_p, x_q)], \quad (31)$$

where $s_{\text{Gauss;1}}(t_p, x_q) \sim \mathcal{N}(0,1)$ and $s_{\text{Gauss;2}}(t_p, x_q) \sim \mathcal{N}(0,1)$. The second step is the application of a low-pass filtering in the range-direction, for each acquisition q. Indeed, for each acquisition, the generation of an uncorrelated random sequence over the discrete time (8) effectively create a noise with bandwidth f_s, and the signal must be low-pass filtered to have the desired bandwidth. In our simulation, we reduce the bandwidth of the noise to that of the instrument, B_w, in order to mimic the frequency selectivity of the radar. Consequently, as those signals are used in eqs. (10)-(11) at a central frequency f_0, the effective spectrum of the signal covers the $[f_0 - \frac{B_w}{2}, f_0 + \frac{B_w}{2}]$ interval.

B. LWA1 complex data

The time-domain signals provided by the LWA1 radiotelescope are uncallibrated complex waveforms.

Let $J_{\text{LWA1}}(m,n)$ be the original bidimensional sampled waveform. The number of fast-time bins is fixed at 4096, and the number of acquisitions N_{acq} depends on the recording, thus we write $m = [1, 2, ..., 4096]$ and $n = [1, 2, ..., N_{\text{acq}}]$.

1) Low-pass filtering: The LWA1 signals that we have considered have a frequency content that ranges from 10.2 to 29.8 MHz (corresponding to a bandwidth of 19.6 MHz). The signals are low-pass filtered so that their bandwidth is equivalent to that of the target instrument, 2.8 MHz in the case of RIME. This is done by setting to zero all spectral content above 13 MHz, which corresponds to the 586th sample in our case. Let $\tilde{J}(m,n) \equiv \mathcal{F}_m\{J_{\text{LWA1}}(m,n)\}$ be the Fourier transform of the original signal in the fast-time direction. We write

$$J_1(m,n) = \mathcal{F}_m^{-1}\left\{\tilde{J}(m,n) \times K(m,n)\right\} \quad (32)$$

where $\times$ is understood as element-wise multiplication and $K(m,n) = 0$ for $m < 587$ and 1 otherwise, $\forall n$.

2) Interpolation: The signal $J_1(m,n)$ has a sampling period of $T_{\text{LWA1}} = (19.6\times10^6)^{-1}$ s and a pulse repetition interval of $\text{PRI}_{\text{LWA1}} = 21$ ms. In order to be used as the transmitted signal of a given radar instrument, those intervals must be adapted to those of that instrument. Due to the large PRF of these files, a decimation step in the along-track direction (*i.e.*, keeping one range line of out ten) is first applied, reducing the PRF to 478.5 Hz. The remaining matching is done by interpolation. Denoting the interpolant $\mathcal{L}(\cdot)$, we write

$$s_{\text{LWA1}}(t_p, x_q) = \mathcal{L}\{J_2(m,n)\} \quad (33)$$

where $t_p = pT_s$ and $x_q = qvT_a$ represent the adequately sampled time-delay and acquisition axes.

REFERENCES

[1] Sune RJ Axelsson. Noise radar for range/doppler processing and digital beamforming using low-bit adc. *IEEE Transactions on Geoscience and Remote Sensing*, 41(12):2703–2720, 2003.

[2] Sune RJ Axelsson. Noise radar using random phase and frequency modulation. *IEEE Transactions on Geoscience and Remote Sensing*, 42(11):2370–2384, 2004.

[3] Y Berquin, W Kofman, A Herique, G Alberti, and P Beck. A study on ganymede's surface topography: Perspectives for radar sounding. *Planetary and Space Science*, 77:40–44, 2013.

[4] Yann Berquin, Alain Herique, Wlodek Kofman, and Essam Heggy. Computing low-frequency radar surface echoes for planetary radar using huygens-fresnel's principle. *Radio Science*, 50(10):1097–1109, 2015. 2015RS005714.

[5] Donald D Blankenship, Duncan A Young, William B Moore, and John C Moore. Radar sounding of europa's subsurface properties and processes: The view from earth. *Europa. University of Arizona Press, Tucson, AZ*, 2009.

[6] L. Bruzzone, G. Alberti, C. Catallo, A. Ferro, W. Kofman, and R. Orosei. Subsurface radar sounding of the jovian moon ganymede. *Proceedings of the IEEE*, 99(5):837–857, May 2011.

[7] TD Carr, MD Desch, and JK Alexander. Phenomenology of magnetospheric radio emissions. *Physics of the jovian magnetosphere*, 1983.

[8] L Carrer, DM Schroeder, A Romero-Wolf, P Ries, and L Brurzone. Noise character constraints on passive radio sounding of jupiter's icy moons using jovian decametric radiation. In *IGARSS 2018-2018 IEEE International Geoscience and Remote Sensing Symposium*, pages 4158–4161. IEEE, 2018.

[9] B Cecconi, S Hess, A Hérique, MR Santovito, D Santos-Costa, P Zarka, G Alberti, D Blankenship, J-L Bougeret, L Bruzzone, et al. Natural radio emission of jupiter as interferences for radar investigations of the icy satellites of jupiter. *Planetary and Space Science*, 61(1):32–45, 2012.

[10] TE Clarke, CA Higgins, Jinhie Skarda, Kazumasa Imai, Masafumi Imai, Francisco Reyes, Jim Thieman, Ted Jaeger, Henrique Schmitt, Nagini Paravastu Dalal, et al. Probing jovian decametric emission with the long wavelength array station 1. *Journal of Geophysical Research: Space Physics*, 119(12):9508–9526, 2014.

[11] SW Ellingson, GB Taylor, J Craig, J Hartman, J Dowell, CN Wolfe, TE Clarke, BC Hicks, NE Kassim, PS Ray, et al. The lwa1 radio telescope. *IEEE Transactions on Antennas and Propagation*, 61(5):2540–2549, 2013.

[12] WenZhe Fa and YaQiu Jin. Simulation of radar sounder echo from lunar surface and subsurface structure. *Science China Earth Sciences*, 53(7):1043–1055, 2010.

[13] R.L Fergason, T.M. Hare, and J. Laura. Hrsc and mola blended digital elevation model at 200m v2. *Astrogeology PDS Annex, U.S. Geological Survey*, 2018.

[14] C. Gerekos, A. Tamponi, L. Carrer, D. Castelletti, M. Santoni, and L. Bruzzone. A coherent multilayer simulator of radargrams acquired by radar sounder instruments. *IEEE Transactions on Geoscience and Remote Sensing*, pages 1–17, 2018.

[15] Essam Heggy, Giovanni Scabbia, Lorenzo Bruzzone, and Robert T Pappalardo. Radar probing of jovian icy moons: Understanding subsurface water and structure detectability in the juice and europa missions. *Icarus*, 285:237–251, 2017.

[16] Paul E Howland, D Maksimiuk, and G Reitsma. Fm radio based bistatic radar. *IEE Proceedings-Radar, Sonar and Navigation*, 152(3):107–115, 2005.

[17] Masafumi Imai, Kazumasa Imai, Charles A Higgins, and James R Thieman. Comparison between cassini and voyager observations of jupiter's decametric and hectometric radio emissions. *Journal of Geophysical Research: Space Physics*, 116(A12), 2011.

[18] KK Khurana, MG Kivelson, DJ Stevenson, G Schubert, CT Russell, RJ Walker, and C Polanskey. Induced magnetic fields as evidence for subsurface oceans in europa and callisto. *Nature*, 395(6704):777, 1998.

[19] Jin Au Kong. Theory of electromagnetic waves. *New York, Wiley-Interscience, 1975.*, 1975.

[20] A Kumamoto, Y Kasaba, F Tsuchiya, H Misawa, H Kita, W Puccio, J-E Wahlund, J Bergman, B Cecconi, Y Goto, et al. Feasibility of the exploration of the subsurface structures of jupiter's icy moons by interference of jovian hectometric and decametric radiation. 2017.

[21] WS Kurth, GB Hospodarsky, DL Kirchner, BT Mokrzycki, TF Averkamp, WT Robison, CW Piker, M Sampl, and P Zarka. The juno waves investigation. *Space Science Reviews*, 213(1-4):347–392, 2017.

[22] Mateusz Malanowski and Krzysztof Kulpa. Two methods for target localization in multistatic passive radar. *IEEE transactions on Aerospace and Electronic Systems*, 48(1):572–580, 2012.
[23] Jeremie Mouginot, Wlodek Kofman, Ali Safaeinili, and Alain Hérique. Correction of the ionospheric distortion on the marsis surface sounding echoes. *Planetary and Space Science*, 56(7):917–926, 2008.
[24] F Nimmo and PM Schenk. Stereo and photoclinometric comparisons and topographic roughness of europa. In *Lunar and Planetary Science Conference*, volume 39, page 1464, 2008.
[25] T. Ono, A. Kumamoto, Y. Kasahara, Y. Yamaguchi, A. Yamaji, T. Kobayashi, S. Oshigami, H. Nakagawa, Y. Goto, K. Hashimoto, Y. Omura, T. Imachi, H. Matsumoto, and H. Oya. The lunar radar sounder (lrs) onboard the kaguya (selene) spacecraft. *Space Science Reviews*, 154(1):145–192, 2010.
[26] S. T. Peters, D. M. Schroeder, D. Castelletti, M. Haynes, and A. Romero-Wolf. In situdemonstration of a passive radio sounding approach using the sun for echo detection. *IEEE Transactions on Geoscience and Remote Sensing*, 56(12):7338–7349, Dec 2018.
[27] G. Picardi, D. Biccari, R. Seu, L. Marinangeli, W.T.K. Johnson, R.L. Jordan, J. Plaut, A. Safaenili, D.A. Gurnett, G.G. Ori, R. Orosei, D. Calabrese, and E. Zampolini. Performance and surface scattering models for the mars advanced radar for subsurface and ionosphere sounding (marsis). *Planetary and Space Science*, 52(1–3):149 – 156, 2004. Exploring Mars Surface and its Earth Analogues.
[28] Andrew Romero-Wolf, Dustin M Schroeder, Paul Ries, Bruce G Bills, Charles Naudet, Bryan R Scott, Robert Treuhaft, and Steve Vance. Prospects of passive radio detection of a subsurface ocean on europa with a lander. *Planetary and Space Science*, 129:118–121, 2016.
[29] Andrew Romero-Wolf, Steve Vance, Frank Maiwald, Essam Heggy, Paul Ries, and Kurt Liewer. A passive probe for subsurface oceans and liquid water in jupiter's icy moons. *Icarus*, 248:463–477, 2015.
[30] A Safaeinili, W Kofman, JF Nouvel, A Herique, and RL Jordan. Impact of mars ionosphere on orbital radar sounder operation and data processing. *Planetary and Space Science*, 51(7-8):505–515, 2003.
[31] Dustin M Schroeder, Andrew Romero-Wolf, Leonardo Carrer, Cyril Grima, Bruce A Campbell, Wlodek Kofman, Lorenzo Bruzzone, and Donald D Blankenship. Assessing the potential for passive radio sounding of europa and ganymede with rime and reason. *Planetary and Space Science*, 134:52–60, 2016.
[32] R. Seu, D. Biccari, R. Orosei, L.V. Lorenzoni, R.J. Phillips, L. Marinangeli, G. Picardi, A. Masdea, and E. Zampolini. Sharad: The {MRO} 2005 shallow radar. *Planetary and Space Science*, 52(1–3):157 – 166, 2004. Exploring Mars Surface and its Earth Analogues.
[33] Merrill Ivan Skolnik. Introduction to radar systems. *New York, McGraw Hill Book Co., 1980. 590 p.*, 1980.
[34] Tilman Spohn and Gerald Schubert. Oceans in the icy galilean satellites of jupiter? *Icarus*, 161(2):456–467, 2003.
[35] RIME Team. Rime instrument scientific performance report, issue 4. *Internal report*, 2018.
[36] Q. Taupin under direction of W. Kofman. Étude d'un radar passif pour le sondage de ganymède et d'europe. *Internship report*, IPAG UGA/CNRS 2018.
[37] P Zarka, B Cecconi, and WS Kurth. Jupiter's low-frequency radio spectrum from cassini/radio and plasma wave science (rpws) absolute flux density measurements. *Journal of Geophysical Research: Space Physics*, 109(A9), 2004.
[38] Philippe Zarka. Auroral radio emissions at the outer planets: Observations and theories. *Journal of Geophysical Research: Planets*, 103(E9):20159–20194, 1998.